

PAPER • OPEN ACCESS

Omnidirectional angle constraint based dynamic six-degree-of-freedom measurement for spacecraft rendezvous and docking simulation

To cite this article: Shendong Shi *et al* 2018 *Meas. Sci. Technol.* **29** 045005

View the [article online](#) for updates and enhancements.

You may also like

- [Trajectory control with continuous thrust applied to a rendezvous maneuver](#)
W G Santos and E M Rocco
- [Entangled rendezvous: a possible application of Bell non-locality for mobile agents on networks](#)
P Mironowicz
- [Rendezvous of a continuous low-thrust cubesat with a satellite](#)
Badaoui El Mabsout, Pierre Claudé and Michel Dudeck

Omnidirectional angle constraint based dynamic six-degree-of-freedom measurement for spacecraft rendezvous and docking simulation

Shendong Shi¹, Linghui Yang¹, Jiarui Lin, Yongjie Ren, Siyang Guo¹ and Jigui Zhu

State Key Laboratory of Precision Measuring Technology and Instruments, Tianjin University, Tianjin 300072, People's Republic of China

E-mail: icelinker@tju.edu.cn

Received 20 September 2017, revised 24 November 2017

Accepted for publication 15 December 2017

Published 28 February 2018



Abstract

In this paper we present a novel omnidirectional angle constraint based method for dynamic 6-DOF (six-degree-of-freedom) measurement. A photoelectric scanning measurement network is employed whose photoelectric receivers are fixed on the measured target. They are in a loop distribution and receive signals from rotating transmitters. Each receiver indicates an angle constraint direction. Therefore, omnidirectional angle constraints can be constructed in each rotation cycle. By solving the constrained optimization problem, 6-DOF information can be obtained, which is independent of traditional rigid coordinate system transformation. For the dynamic error caused by the measurement principle, we present an interpolation method for error reduction. Accuracy testing is performed in an 8×8 m measurement area with four transmitters. The experimental results show that the dynamic orientation RMSEs (root-mean-square errors) are reduced from 0.077° to 0.044° , 0.040° to 0.030° and 0.032° to 0.015° in the X, Y, and Z axes, respectively. The dynamic position RMSE is reduced from 0.65 mm to 0.24 mm. This method is applied during the final approach phase in the rendezvous and docking simulation. Experiments under different conditions are performed in a 40×30 m area, and the method is verified to be effective.

Keywords: dynamic 6-DOF measurement, omnidirectional angle constraint, dynamic error, transmitter synchronization, rendezvous and docking simulation

(Some figures may appear in colour only in the online journal)

1. Introduction

In recent years, autonomous spacecraft rendezvous and docking technology has been a popular research topic because of its essentiality in spacecraft control. The measurement accuracy, volume and mass of the measurement unit are

crucial concerns in this field [1]. Our work is focused on all aspects, attempting to both improve the measurement accuracy and miniaturize the sensor unit.

Several methods have been proposed such as INS (inertial navigation system), photogrammetry, LIDAR, and laser tracker. However, on account of the integral operation, the measurement errors of INS accumulate over time, and it is prone to drift. Some compensation methods have been proposed to reduce the measurement error, but they are not ideal in practice because of the compensation uniqueness [2–5]. As a result, INS is rarely used alone.

¹ Author to whom any correspondence should be addressed.



Original content from this work may be used under the terms of the [Creative Commons Attribution 3.0 licence](https://creativecommons.org/licenses/by/3.0/). Any further distribution of this work must maintain attribution to the author(s) and the title of the work, journal citation and DOI.

Photogrammetry provides alternative solutions for 6-DOF (six-degree-of-freedom) measurement based on a single-camera or multiple-cameras. Hui *et al* introduced a 6-DOF estimation algorithm for cooperative space targets based on monocular vision [6]. You *et al* developed a binocular vision system for spacecraft positioning. The maximum standard deviation was less than 2 mm in 4 m [7]. Feng *et al* proposed a stereo-vision-based relative orientation estimation method for the rendezvous and docking of non-cooperative satellites. The position error was 6.4 mm and attitude angle error exceeds 0.34° [8]. Dahlin demonstrated a vision navigation method for orbital rendezvous and docking. The angle error was within 0.1° but the position error exceeded 25 mm [9]. Photogrammetry method has better accuracy and stability than INS. Nevertheless, it is easily affected by light interference and object occlusion. Meanwhile, photogrammetry method is based on image processing, which is often time-consuming and results in poor dynamic measurement capability.

The emergence of LIDAR has led to a new generation of vision-based rendezvous and docking measurement systems. Ruel *et al* demonstrated an active TriDAR (triangulation + LIDAR) 3D sensor and efficient model-based tracking algorithm to provide 6-DOF information about the spacecraft. The position error was 28.9 mm and the attitude angle error was 1.3° [10]. Jasiobedzki *et al* developed an autonomous satellite rendezvous and docking measurement method using LIDAR and model-based vision. The maximum translation and rotation errors were 4.4 mm and 0.25° respectively [11]. LIDAR has the longest measurement range, but it is usually hard to delivery high absolute accuracy.

6-DOF probe cooperated with laser tracker is another method that has been developed commercially, such as T-mac [12]. It is noted for its high accuracy and fast dynamic response. It is often used as benchmark. In large space, multiple stations are needed because for measurement visibility. Nonetheless, laser trackers are extremely expensive and have certain requirements on their working environment. The measurement efficiency is relatively low.

Combined measurement methods are also widely used [13–17]. Ideally, the position error is meter-level and the orientation error exceeds 0.3° outdoors. Qu *et al* designed a real-time measurement system with vision/INS for close-range semi-physical rendezvous and docking simulation. The standard deviation in the relative position was 6.4 mm and the standard deviations in the relative attitude angles were within 0.0315° [18]. The combined measurement methods give full play to the advantages of each subsystem and avoids the disadvantages, but the complicated calibration and alignment processes prevent its prevalence.

Distributed photoelectric scanning measurement technology has been further studied and developed rapidly in recent years. It has been widely used in digital manufacturing and assembly. wMPS (workshop measurement and positioning system) and iGPS (indoor global positioning system) are examples consisting of transmitters with different rotation speeds, photoelectric receivers, a signal processor, and a terminal computer. With the advantages of high accuracy, fast response, multi-tasking and strong extensibility, they

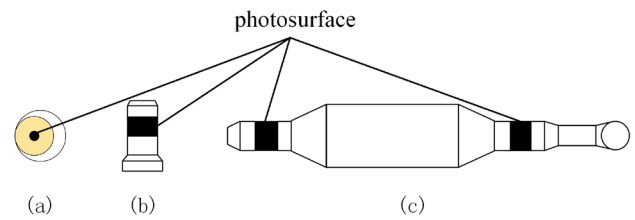


Figure 1. Receiving sensors: (a) wMPS receiver (b) iGPS single-photosensitive sensor and (c) iGPS vector bar.

are well received. The spherical receiver of wMPS (figure 1(a)) is 38.1 mm in diameter and interchangeable with the laser tracker spherically-mounted retroreflector (SMR). The machining accuracy is 0.02 mm and the alignment accuracy of the photosurface is better than 0.01 mm. The receiving sensors of iGPS have two types: the single-photosurface sensor (figure 1(b)) and the vector bar (figure 1(c)).

Unlike single-station measurement systems such as the total station and laser tracker, the accuracy of a distributed measurement network is determined by the transmitter distribution rather than the measurement distance. The accuracy increases if more signals are received. Station transformation and error accumulation are avoided. Generally, wMPS and iGPS output the 3D coordinates of the static measured receiver if it obtains signals from more than two transmitters. As for a dynamic receiver, the measurement error is extremely obvious and non-negligible.

Based on coordinate calculations and rigid body transformations, iGPS can be used for 6-DOF measurement. However, this method may fail to work in restricted space because of laser plane intersection failure. We propose a novel dynamic 6-DOF measurement method for spacecraft rendezvous and docking simulation based on omnidirectional angle constraint. Photoelectric receivers are fixed to the measured spacecraft and they are in a loop distribution. Each receiver indicates an angle constraint direction. With the spacecraft moving in the measurement space, the photoelectric receivers obtain signals from the rotating transmitter lasers. Omnidirectional angle constraint equations can then be established. If each receiver obtains the signal from at least one transmitter, the 6-DOF of the spacecraft can be calculated iteratively with the optimization algorithm. Independent of coordinate calculation and rigid body transformation, omnidirectional angle constraint method has stronger applicability than iGPS. The calibration of measurement network can be finished within 20 min and the accuracy is traced to length benchmark in industrial site. For the dynamic error caused by receiver movement, an interpolation method is introduced to improve the dynamic accuracy. Experiments have verified its effectiveness.

This paper is organized as follows: section 2 introduces the wMPS measurement model and network construction. Section 3 presents the 6-DOF measurement principle and mathematical solution. Section 4 describes the interpolation method to synchronize transmitters and reduce the dynamic measurement error. In section 5, two experiments are conducted to test the proposed method. Finally, we present the conclusions and prospects for future improvement.

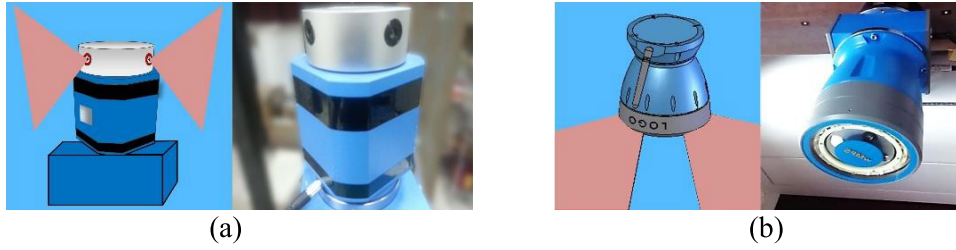


Figure 2. Transmitter configuration (a) floor transmitter and (b) roof transmitter.

2. Measurement model and network construction

Each transmitter consists of a rotating head and a static base. Two linear laser modules are fixed in the rotating head and emit planar laser beams (scanning signals) with an angle of 90° between them. In the base, several synchronization laser modules are distributed circumferentially and emit pulses (synchronization signals). The floor transmitter has a typical configuration, located on a tripod (figure 2(a)). The scanning angle is 0–360° horizontally and –22.5° to +22.5° vertically. The floor transmitter is similar to the iGPS transmitter. In this paper, the marble platform used for the rendezvous and docking simulation is about 40 × 30 m. We designed the roof transmitter (figure 2(b)) considering the application environment and light occlusion caused by other equipment, which is unsupported for iGPS.

The roof transmitter emits laser beams downward. The coefficients for each plane $a_{ki}b_{ki}c_{ki}d_{ki}$ (i : laser plane index and k : transmitter index) are calibrated after the transmitter is assembled. The transmitter coordinate system, also called the local coordinate system (LCS), is defined as follows: the axis of rotation is Z-axis. The intersection point of plane 1 and the Z-axis is defined as the origin O . The X-axis is in plane 1 at the initial time and vertical with respect to Z-axis. The direction of Y-axis is determined according to the right-hand rule. The photoelectric receiver can be seen as a mass point. When the transmitter works, the head rotates counterclockwise at the speed of 25–50 rev s⁻¹ (revolutions/second). Each time plane 1 rotates across the initial position, the receiver obtains the synchronization signals and records the initial time t_k . The time when the receiver obtains the scanning signals (plane 1 and plane 2) is recorded as t_{k1} and t_{k2} . Then the rotation angle is described by:

$$\begin{cases} \theta_{k1} = \omega_k (t_{k1} - t_k) \\ \theta_{k2} = \omega_k (t_{k2} - t_k) \end{cases} \quad (2.1)$$

ω_k represents the rotational angular speed of transmitter k . The parameters of planes 1 and 2 in the LCS are changed:

$$\begin{bmatrix} a_{ki\theta} \\ b_{ki\theta} \\ c_{ki\theta} \\ d_{ki\theta} \end{bmatrix} = \begin{bmatrix} \cos \theta_{ki} & -\sin \theta_{ki} & 0 & 0 \\ \sin \theta_{ki} & \cos \theta_{ki} & 0 & 0 \\ 0 & 0 & 1 & 0 \\ 0 & 0 & 0 & 1 \end{bmatrix} \begin{bmatrix} a_{ki} \\ b_{ki} \\ c_{ki} \\ d_{ki} \end{bmatrix} \quad (2.2)$$

For an observed point (x_l, y_l, z_l) in the LCS, the equations of planes 1 and 2 can be listed as follows:

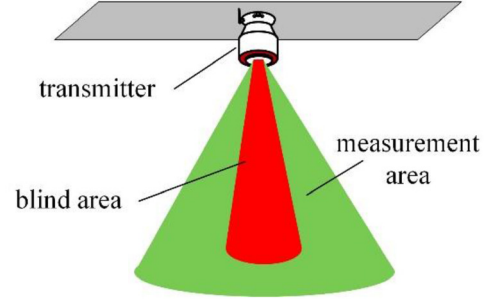


Figure 3. Measurement and blind areas for the roof transmitter.

Table 1. Transmitter location in the GCS.

NO.	X			Z			
	(mm)	Y (mm)	(mm)	NO.	X (mm)	Y (mm)	Z (mm)
1	9000	13000	9000	6	15000	25000	9000
2	15000	7000	9000	7	27000	25000	9000
3	27000	7000	9000	8	33000	19000	9000
4	33000	13000	9000	9	21000	13000	9000
5	9000	19000	9000	10	21000	19000	9000

$$\begin{cases} a_{k1\theta}x_l + b_{k1\theta}y_l + c_{k1\theta}z_l + d_{k1\theta} = 0 \\ a_{k2\theta}x_l + b_{k2\theta}y_l + c_{k2\theta}z_l + d_{k2\theta} = 0 \end{cases} \quad (2.3)$$

Generally, the coordinates in the global coordinate system (GCS) are more meaningful than those in the LCS. Therefore, the orientation and position relationship from the GCS to the LCS is calibrated, described by:

$$\begin{bmatrix} x_l \\ y_l \\ z_l \\ 1 \end{bmatrix} = \begin{bmatrix} R_{gl} & T_{gl} \\ 0 & 1 \end{bmatrix} \begin{bmatrix} x_g \\ y_g \\ z_g \\ 1 \end{bmatrix} \quad (2.4)$$

R_{gl} and T_{gl} are the rotation and translation matrices from the GCS to the LCS respectively. If a receiver obtains signals from more than two transmitters, the coordinates (x_g, y_g, z_g) can be determined. The coordinate accuracy is positively correlated with the number of transmitters scanning over the receiver.

According to the model in figure 3, the roof transmitter has a cone projection area of 53°, in which 15° is the blind area. The rotational speed stability of the roof transmitter is within ± 1 rev min⁻¹ and the angle measurement accuracy is better than 2 arc seconds. The operating distance of the roof transmitter is 5–25 m.

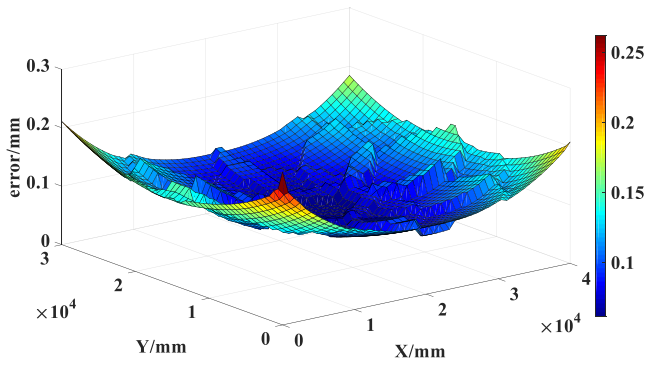


Figure 4. Simulation results for ten-transmitter network.

To evaluate the distribution of accuracy in 40×30 m area, a Monte-Carlo simulation of the accuracy is made. The layout of the ten transmitters in the GCS and the simulation results are listed in table 1 and figure 4:

The effective measurement zone in this layout almost covers the entire 40×30 m area, and the simulation errors in most of the region are better than 0.15 mm. The maximum error is less than 0.25 mm. The layout satisfies the measurement requirements.

3. Principle of 6-DOF measurement

3.1. Spacecraft coordinate system construction

To measure the 6-DOF information, it is necessary to construct a coordinate system on the measured spacecraft. On the top of the spacecraft, six receivers are fixed as reference points. The coordinates of the reference points are measured by the laser tracker at four different positions as depicted in figure 5. The distance and angular errors are optimized according to the constraints provided by the laser tracker. The coordinates of

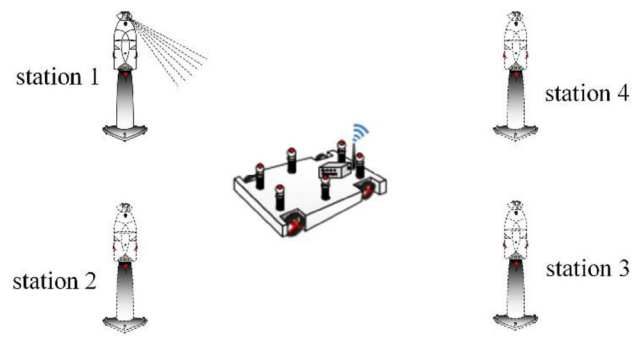


Figure 5. Construction of the spacecraft coordinate system.

Receivers on the spacecraft obtain the signals when the laser beams scan over them. For example, when receiver m captures the signals of transmitter k , the coefficients of planes 1 and 2 in transmitter k are updated according to (2.2). Transform the updated plane equations from the LCS of transmitter k to the GCS:

$$[a_{gki\theta} b_{gki\theta} c_{gki\theta} d_{gki\theta}] = [a_{ki\theta} b_{ki\theta} c_{ki\theta} d_{ki\theta}] \begin{bmatrix} R_{klg} & T_{klg} \\ 0 & 1 \end{bmatrix}^{-1}. \quad (3.3)$$

For receiver m (x_m, y_m, z_m) in the spacecraft coordinate system, the distance between the reference point and the laser plane can be defined as:

$$d_{mki} = \left\| \left[a_{gki\theta} b_{gki\theta} c_{gki\theta} d_{gki\theta} \right] \begin{bmatrix} R & T \\ 0 & 1 \end{bmatrix} \cdot \begin{bmatrix} x_m \\ y_m \\ z_m \\ 1 \end{bmatrix} \right\|_2. \quad (3.4)$$

In the equation above, the unknowns are rotation matrix R and translation matrix T which indicate the transformation from the spacecraft LCS to the GCS. θ , γ and ψ are Euler angles.

$$R = \begin{bmatrix} r_{11} & r_{12} & r_{13} \\ r_{21} & r_{22} & r_{23} \\ r_{31} & r_{32} & r_{33} \end{bmatrix} = \begin{bmatrix} \cos\gamma * \cos\psi & \cos\psi * \sin\theta * \sin\gamma - \cos\theta * \sin\psi & \sin\theta * \sin\psi + \cos\theta * \cos\psi * \sin\gamma \\ \cos\gamma * \sin\psi & \cos\theta * \cos\psi + \sin\theta * \sin\gamma * \sin\psi & \cos\theta * \sin\gamma * \sin\psi - \cos\psi * \sin\theta \\ -\sin\gamma & \cos\gamma * \sin\theta & \cos\theta * \cos\gamma \end{bmatrix} \quad (3.5)$$

the reference points (x_m, y_m, z_m) in the spacecraft coordinate system can be obtained [19].

3.2. Algorithm and optimization

According to (2.4), the transformation from the LCS to the GCS can be expressed as:

$$R_{lg} = R_{gl}^{-1} \quad (3.1)$$

$$T_{lg} = -R_{gl}^{-1} T_{gl}. \quad (3.2)$$

$$T = [t_x t_y t_z]^T. \quad (3.6)$$

Furthermore, due to the orthogonality of the rotation matrix, (3.5) satisfies the equations below:

$$f_j = r_{p1} r_{q1} + r_{p2} r_{q2} + r_{p3} r_{q3} = \begin{cases} 0 & p \neq q \\ 1 & p = q \end{cases}. \quad (3.7)$$

The 6-DOF measurement problem can be formulated as an optimization based on the penalty function method. The objective function can be described by:

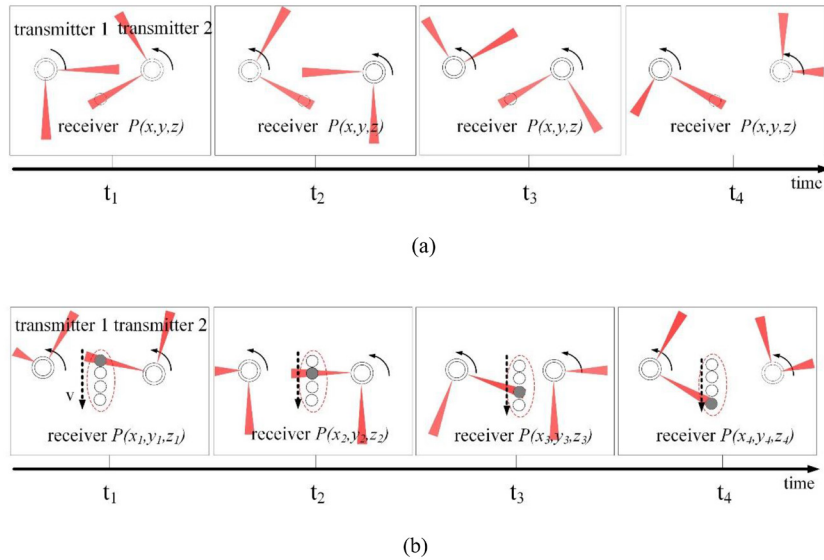


Figure 6. Measurement processes for (a) static receiver and (b) dynamic receiver.

$$F = \sum_{m=1}^M \sum_{k=1}^N \sum_{i=1}^2 (d_{mki})^2 + \lambda \sum_{j=1}^6 \begin{cases} f_j^2 & p \neq q \\ (f_j - 1)^2 & p = q \end{cases} \quad (3.8)$$

Only if each receiver obtains the signal of at least one transmitter can, the optimization problem be resolved by the Levenberg–Marquardt algorithm [20]. The attitude angle can be calculated through R , and the position information is in T .

In the measurement process, receivers may get the signals from transmitters in the entire space. Generally, the accuracy of the optimization result is positively correlated with the number of signals each receiver obtains.

3.3. Initial iteration value calculation

For the Levenberg–Marquardt algorithm, it is necessary to provide a proper initial iteration value to make the optimization result convergent and reduce the iteration times. d_{mki} can be expanded and constitute a system of equations such that $AX = D$

$$A = \begin{bmatrix} a_{g1\theta 1}x_m & a_{g1\theta 1}y_m & a_{g1\theta 1}z_m & b_{g1\theta 1}x_m & b_{g1\theta 1}y_m & b_{g1\theta 1}z_m & c_{g1\theta 1}x_m & c_{g1\theta 1}y_m & c_{g1\theta 1}z_m & a_{g1\theta 1} & b_{g1\theta 1} & c_{g1\theta 1} \\ a_{g1\theta 2}x_m & a_{g1\theta 2}y_m & a_{g1\theta 2}z_m & b_{g1\theta 2}x_m & b_{g1\theta 2}y_m & b_{g1\theta 2}z_m & c_{g1\theta 2}x_m & c_{g1\theta 2}y_m & c_{g1\theta 2}z_m & a_{g1\theta 2} & b_{g1\theta 2} & c_{g1\theta 2} \\ \dots & \dots & \dots & \dots & \dots & \dots & \dots & \dots & \dots & \dots & \dots & \dots \\ a_{gk\theta 1}x_m & a_{gk\theta 1}y_m & a_{gk\theta 1}z_m & b_{gk\theta 1}x_m & b_{gk\theta 1}y_m & b_{gk\theta 1}z_m & c_{gk\theta 1}x_m & c_{gk\theta 1}y_m & c_{gk\theta 1}z_m & a_{gk\theta 1} & b_{gk\theta 1} & c_{gk\theta 1} \\ a_{gk\theta 2}x_m & a_{gk\theta 2}y_m & a_{gk\theta 2}z_m & b_{gk\theta 2}x_m & b_{gk\theta 2}y_m & b_{gk\theta 2}z_m & c_{gk\theta 2}x_m & c_{gk\theta 2}y_m & c_{gk\theta 2}z_m & a_{gk\theta 2} & b_{gk\theta 2} & c_{gk\theta 2} \end{bmatrix} \quad (3.9)$$

$$X = [r_{11}r_{12}r_{13}r_{21}r_{22}r_{23}r_{31}r_{32}r_{33}t_x t_y t_z]^T \quad (3.10)$$

$$D = [d_{111}d_{112} \dots d_{mk1}d_{mk2}]^T \quad (3.11)$$

In the transmitter model, X -axis is located in plane 1, so d_{mk1} should be zero. Additionally, with the assembly technique, plane 2 can be adjusted to the position that approximately

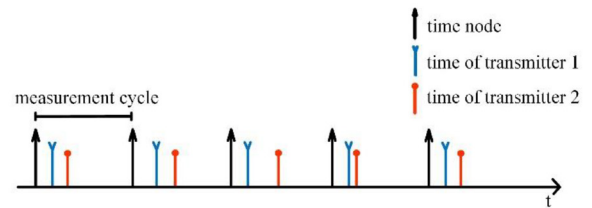


Figure 7. Timed shaft for measurement data (two transmitters).

passes through the original O . d_{mk2} can also be seen to be zero. Thus, the initial value X can be produced by solving the homogeneous linear equation system:

$$AX = 0. \quad (3.12)$$

By the singular value decomposition on A , matrices U and V can be obtained. According to the least squares principle, the singular vector in matrix V corresponding to the minimum singular value in matrix S is the least squares solution of (3.12).

The initial value of the iteration is now produced. Substituting it into the object function, the 6-DOF measurement can be solved.

4. Dynamic error and reduction

In 6-DOF measurement, the dynamic error is mainly caused by the measurement principle. The raw data is the time when



Figure 8. Experiment platform for dynamic 6-DOF measurement.

the receiver obtains the synchronization signals and scanning signals from different transmitters. During the movement of the spacecraft, a receiver gets signals from more than one transmitter. However, each transmitter emits synchronization signals at different times, and the scanning signals also reach the receiver in a certain order. Thus, the dynamic receiver is in different positions during a measurement process, which may cause absolute errors. Take two transmitters for example. Figures 6(a) and (b) show the measurement process for static and dynamic receivers.

Essentially, the dynamic error is caused by the time differences between the synchronization signals and the scanning signals. It is affected by the velocity and the rotational speed of the transmitters. In the first case, experiments about the relationship of the velocity and dynamic error have already been done. They have a linear relationship, which agrees with the Matlab simulation results. The error will get larger with increasing the velocity. Secondly, the dynamic error is negatively related with the rotating speed. However, the transmitter shaft will suffer severe abrasion and the lifetime of components will decrease with high rotational speeds. Taking into account these factors, it is set as 25–50 rev s⁻¹. To reduce the measurement error, an effective way is to build a timed shaft and set a series of time nodes according to the measurement frequency, as is shown in figure 7. Calculating the rotation angles of each transmitter at the time nodes, transmitter synchronization can be achieved.

It has been verified by experiments that the scanning times t_{k1} and t_{k2} will be continuous and smooth if the trajectory of the receiver is continuous. Based on this conclusion, Lagrange's interpolation is applied to calculate the scanning angle at any time. The interpolation polynomial is written as:

$$L_n(t) = \sum_{j=0}^n \theta_j l_j(t) = \sum_{j=0}^n \left[\prod_{\substack{i=0 \\ i \neq j}}^n \left(\frac{t-t_i}{t_j-t_i} \right) \right] \theta_j. \quad (4.1)$$

$L_n(t)$ is used to replace the actual polynomial. The interpolation error is described by:

$$R_n(t) = \frac{f^{(n+1)}(\xi)}{(n+1)!} \omega_{n+1}(t), t_a < \xi < t_b \quad (4.2)$$

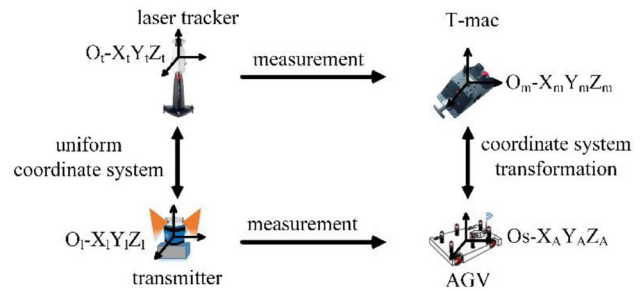


Figure 9. Coordinate system transformation relationship.

$$\omega_{n+1}(t) = \prod_{j=0}^n (t-t_j). \quad (4.3)$$

Taking equidistant interpolation for instance,

$$t = t_a + kh (k = 1, 2 \dots) \quad (4.4)$$

$$\omega_{n+1}(x) = \omega_{n+1}(t_a + kh) = k(k-1) \dots (k-n) h^{n+1}. \quad (4.5)$$

With increasing the interpolation interval h , the interpolation error $R_n(t)$ will also increase. To avoid the Runge's phenomenon, the error decreases with the increasing of n , but the calculation will become more complicated [21]. Weighing these factors, we choose n to be 1 or 2:

$n = 1$, the movement of receiver is seen as uniform linear motion.

$$L_1(t) = \frac{t-t_1}{t_0-t_1} \theta_0 + \frac{t-t_0}{t_1-t_0} \theta_1 = \theta_0 + \frac{t-t_0}{t_1-t_0} (\theta_1 - \theta_0) \quad (4.6)$$

$n = 2$, the movement is seen as uniformly variable linear motion.

$$L_2(t) = \frac{(t-t_1)(t-t_2)}{(t_0-t_1)(t_0-t_2)} \theta_0 + \frac{(t-t_0)(t-t_2)}{(t_1-t_0)(t_1-t_2)} \theta_1 + \frac{(t-t_0)(t-t_1)}{(t_2-t_0)(t_2-t_1)} \theta_2. \quad (4.7)$$

In this way, we can obtain the value of the polynomial at any moment and the signals from all transmitters are aligned to the time node. The synchronization error of the dynamic 6-DOF measurement can be reduced.

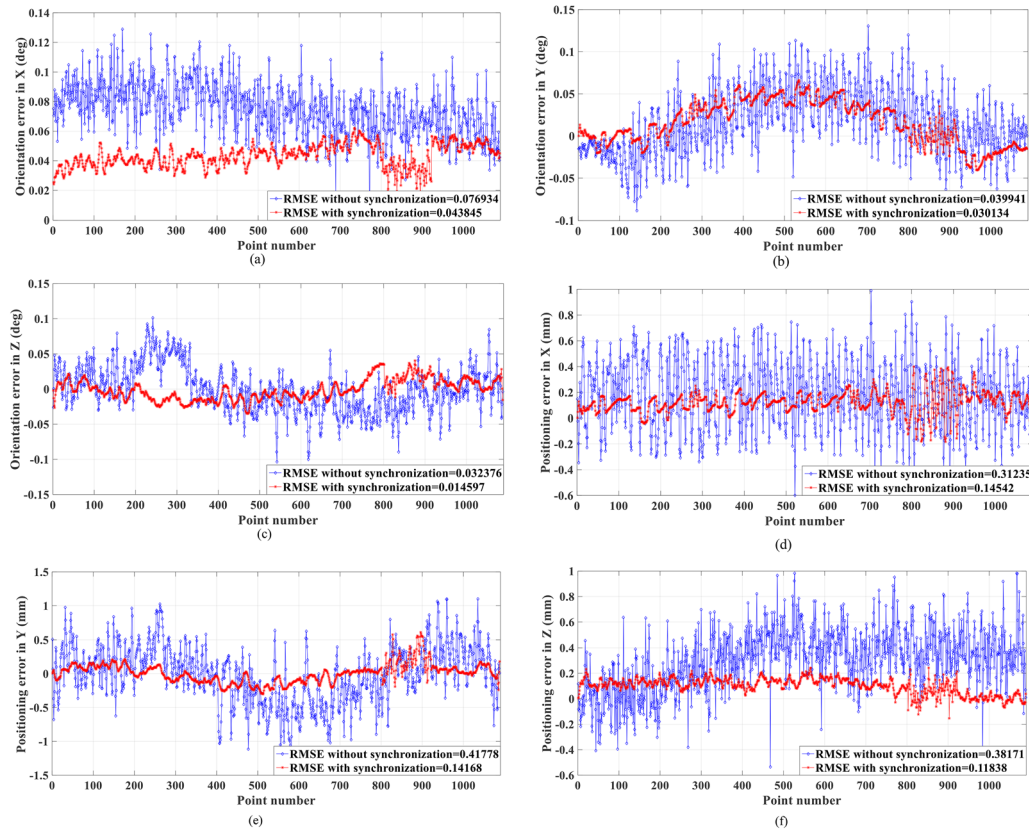


Figure 10. 6-DOF RMSE in the X, Y and Z axes: (a)–(c) orientation RMSEs and (d)–(f) position RMSEs.

Table 2. 6-DOF measurement error analysis.

	Error without synchronization			Error with synchronization		
	Max	Min	Mean	Max	Min	Mean
Orientation in X (°)	0.129	0.0179	0.0751	0.0622	0.0137	0.0432
Orientation in Y (°)	0.1304	−0.0883	0.0157	0.0661	−0.0404	0.0158
Orientation in Z (°)	0.1013	−0.1033	−0.0005	0.0405	−0.0347	−0.0012
Position in X (mm)	0.989	−0.599	0.1782	0.3988	−0.2354	0.1188
Position in Y (mm)	1.1019	−1.3237	−0.0066	0.6159	−0.3031	0.0065
Position in Z (mm)	0.9831	−0.534	0.2982	0.2436	−0.1523	0.1002

5. Experiment

To verify the method for dynamic 6-DOF measurement, two experiments were conducted.

5.1. Accuracy testing experiment

Experiment 1 was conducted for accuracy testing. The experimental setup is shown in figure 8.

Six photoelectric receivers were fixed to the automated guided vehicle (AGV). The coordinate system of the AGV was calibrated according to the method stated in section 3.1. Laser tracker T-mac was also fixed to the AGV. T-mac outputs the 6-DOF information in the laser tracker system. In this experiment it was used as the reference because of its high accuracy in dynamic measurement. Before the experiment, the wMPS measurement field GCS was unified with the laser tracker system. The relative orientation and position of the AGV and

T-mac was also calibrated with the laser tracker. Thus, the outputs of the wMPS and T-mac could be compared in the laser tracker coordinate system after a coordinate system transformation shown in figure 9:

The laser tracker and wMPS were triggered by the software, and the measurement frequency was synchronized at 20 Hz. The AGV was moved along a curvilinear path at a speed of 0.2 m s^{−1}, which was consistent with the maximum velocity of the tracker at the final approach. The experiment was conducted twice: once with synchronization and the other without. The dynamic error is evaluated through root-mean-square errors (RMSEs) given by:

$$RMSE = \sqrt{\frac{\sum_{i=1}^N (x_{i_obs} - x_{i_true})^2}{N}} \tag{5.1}$$

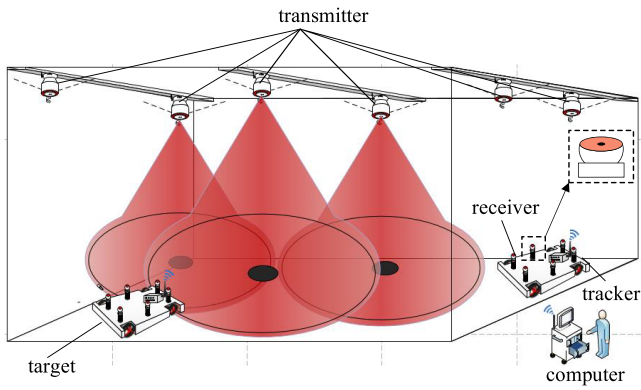


Figure 11. Simplified experiment setup.

Table 3. Coordinates of the six receivers on the tracker.

No.	X (mm)	Y (mm)	Z (mm)
1	26.50574	90.78495	-717.903
2	-1341.47	-107.701	-347.504
3	-672.933	-132.863	1127.775
4	203.7144	-133.301	888.5487
5	703.7625	147.1231	-874.912
6	1080.416	135.9563	-76.005

x_{i_obs} represents the observed value and x_{i_true} represents the true value. N refers to the total number of measurement times.

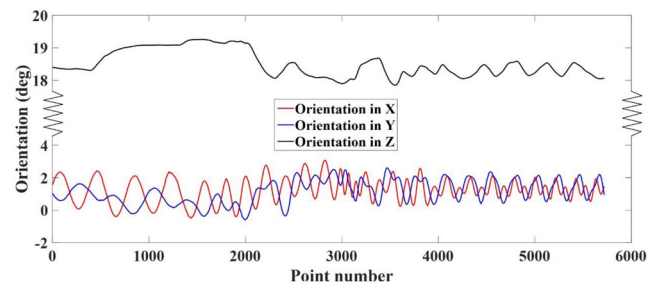
The results compared with the T-mac are listed in figure 10 and table 2:

The curve with rhombi and curve with asterisks represent the measurement errors without and with synchronization, respectively. After transmitter synchronization, the orientation error decreases from 0.077° to 0.044° , 0.040° to 0.030° , 0.032° to 0.015° in each axis. The position error decreases from 0.31 mm to 0.15 mm, 0.42 mm to 0.14 mm, 0.38 mm to 0.12 mm in each axis. The dynamic measurement accuracy is improved and the effectiveness of the proposed method is verified.

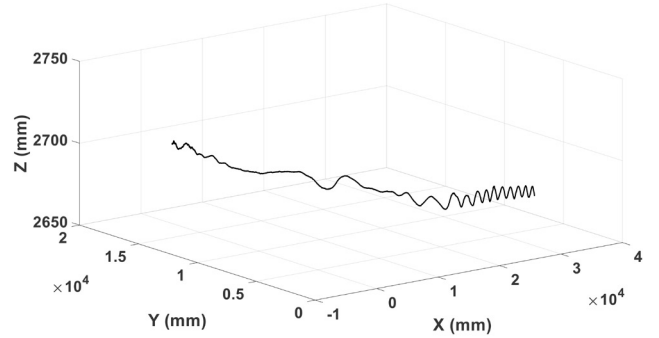
5.2. Spacecraft rendezvous and docking simulation experiment

Experiment 2 was conducted in the rendezvous and docking simulation laboratory. The experimental area is a 40×30 m marble platform. The simplified experiment setup is shown in figure 11.

The tracker and target were placed on the platform. The normal of the platform was parallel to the direction of gravity. The target was static. The tracker has 6-DOF and moves toward the target with the aid of an air-flotation system. The initial speed of the tracker was 0.2 m s^{-1} at the starting point, about 40 m away from the target. It moved along a planned trajectory and experienced two decelerations at distances of 25 m and 10 m; the velocity was reduced to 0.1 m s^{-1} and 0.03 m s^{-1} , respectively. Six receivers were fixed to the top of the tracker. They were arranged horizontally, and the normal of the photosensitive surface was approximately parallel to that of the platform. The coordinates of each receiver in the tracker



(a) Orientation in X, Y and Z axes.



(b) Trajectory of the tracker.

Figure 12. 6-DOF measurement results of the tracker: (a) orientation and (b) trajectory.

coordinate system were calibrated with the Leica AT 901 laser tracker as the method stated in section 3.1. The calibration results are listed in table 3.

The GCS in this experiment was defined as the convention of east-north-up. The position and orientation of the target in the GCS was known before the experiment. When the tracker moved towards the target, the 6-DOF of the target was calculated continuously according to the method above. In the 40×30 m area, each receiver obtained signals from more than two transmitters. The measurement accuracy could be guaranteed this way. Referring to the orientation and position of the target, the tracker adjusted itself in real time. The docking command was sent when the tracker and target were 0.45 m apart. Measurement results throughout the whole process are shown in figure 12.

It is clear that the 6-DOF measurement result curves are continuous and stable. No gross error occurs. The rendezvous and docking process was successfully conducted in different states. The feasibility of this method was verified.

6. Conclusions

Dynamic 6-DOF measurement methods with high accuracy are urgently required in spacecraft rendezvous and docking simulation. Because of the complexity of the problem and on-site situations (e.g. light occlusion), most existing methods fail to achieve a highly accurate measurement. In this paper we propose a novel method based on the omnidirectional angle constraint. The characteristics of dynamic error are analyzed and an interpolation method is proposed to reduce the dynamic error. As the experiments above indicate, the accuracy is improved. In a 40×30 m area, the dynamic 6-DOF




measurement results meet the requirements and provide a basis for feedback control.

In future research, we will focus on improving the measurement frequency and value initialization method. The initial value for optimization can be obtained through the INS for algorithm simplification. The drift error of INS in a short time can be controlled. Moreover, the INS output can also be used for data fusion with wMPS. Thus, the 6-DOF measurement accuracy may be further improved.

Acknowledgments

The work was supported by the National Key Research and Development Project of China (Grant No. 2017YFF0204802), National Natural Science Foundation of China (Grant Nos. 51775380, 51475329), Natural Science Foundation of Tianjin (Grant No. 16JCZDJC38100) and Research Grant of Key Laboratory for Precision and Non-traditional Machining Technology, Ministry of Education, Dalian University of Technology (Grant No. JMTZ201604).

ORCID iDs

Shendong Shi  <https://orcid.org/0000-0002-2490-0578>
 Linghui Yang  <https://orcid.org/0000-0002-9937-1383>
 Siyang Guo  <https://orcid.org/0000-0002-4564-9060>

References

- [1] Burton R, Weston S and Agasid E 2016 State of the art in guidance navigation and control: a survey of small satellite GNC components *Adv. Astronaut. Sci.* **157** 273–82
- [2] Li Z T, Wu T J and Ma L H 2011 A coning compensation algorithm for SINS in high dynamic motion *Control Eng. Appl. Inf.* **13** 32–40
- [3] Yuan B L, Liao D and Han S L 2012 Error compensation of an optical gyro INS by multi-axis rotation *Meas. Sci. Technol.* **23** 025102
- [4] Zhou X, Yang G L, Wang J and Li J 2016 An improved gravity compensation method for high-precision free-INS based on MEC-BP-AdaBoost *Meas. Sci. Technol.* **27** 125007
- [5] Zhang T, Chen K, Fu W X, Yu Y F and Yan J 2014 Optimal two-iteration sculling compensation mathematical framework for SINS velocity updating *J. Syst. Eng. Electron.* **25** 1065–71
- [6] Zhai Y, Zeng L, Xiong W and Shan Q S 2015 Attitude disturbance correction for binocular vision cameras in rendezvous and docking *IEEE Aerosp. Electron. Sys. Mag.* **30** 34–40
- [7] Pan H, Huang J Y and Qin S Y 2013 Relative pose estimation under monocular vision in rendezvous and docking *Appl. Mech. Mater.* **433** 799–805
- [8] Yu F, He Z, Qiao B and Yu X T 2014 Stereo-vision-based relative pose estimation for the rendezvous and docking of noncooperative satellites *Math. Probl. Eng.* **2014** 1–12
- [9] Dahlin E, Woffinden D and Spanos P 2016 Vision navigation performance for autonomous orbital rendezvous and docking *Adv. Astronaut. Sci.* **157** 443–62
- [10] Jasiobedzki P, Se S, Pan T, Umasuthan M and Greenspan M 2005 Autonomous satellite rendezvous and docking using LIDAR and model based vision *Proc. Soc. Photo-Opt. Ins.* **5798** 54–65
- [11] Ruel S, Luu T, Anctil M and Gagnon S 2008 Target localization from 3D data for on-orbit autonomous rendezvous & docking *Aerosp. Conf. Proc.* **2008** 1–11
- [12] Muralikrishnan B, Phillips S and Sawyer D 2016 Laser trackers for large-scale dimensional metrology: a review *Precis. Eng.* **44** 13–28
- [13] Park Y B, Jeon H C and Park C G 2016 Analysis of geometric effects on integrated inertial/vision for lunar descent navigation *J. Guid. Control. Dynam.* **39** 937–43
- [14] Kim S B, Bazin J C, Lee H K, Choi K H and Park S Y 2011 Ground vehicle navigation in harsh urban conditions by integrating inertial navigation system, global positioning system, odometer and vision data *IET Radar. Sonar Navig.* **5** 814–23
- [15] Li M Y and Mourikis A I 2013 High-precision, consistent EKF-based visual-inertial odometry *Int. J. Robot. Res.* **32** 690–711
- [16] Mourikis A I, Trawny N, Roumeliotis S I, Johnson A E, Ansar A and Matthies L 2009 Vision-aided inertial navigation for spacecraft entry, descent, and landing *IEEE Trans. Robot.* **25** 264–80
- [17] Santoso F, Garratt M A and Anavatti S G 2017 Visual-inertial navigation systems for aerial robotics: sensor fusion and technology *IEEE Trans. Autom. Sci. Eng.* **14** 260–75
- [18] Qu Z S, Chu X Y, Fu M Y, Liu X K, Xie W N and Wang C H 2017 Design of real-time measurement system with Vision/IMU for close-range semi-physical rendezvous and docking simulation *IEEE Guidance Navigation and Control Conf.* **2016** 2292–8
- [19] Ren Y, Lin J R, Zhu J G, Sun B and Ye S H 2015 Coordinate transformation uncertainty analysis in large-scale metrology *IEEE Trans. Instrum. Meas.* **64** 2380–8
- [20] Moré J J 1978 The Levenberg–Marquardt algorithm: implementation and theory *Lect. Notes Math.* **630** 105–16
- [21] Epperson J F 1987 On the runge example *Am. Math. Mon.* **94** 329–41